Monthly Notices of the ROYAL ASTRONOMICAL SOCIETY

MNRAS **498,** 2339–2353 (2020) doi:10.1093/mnras/staa2415
Advance Access publication 2020 September 2

The first high-redshift changing-look quasars

Nicholas P. Ross [1]★ Matthew J. Graham [2] Giorgio Calderone,[3] K. E. Saavik Ford,[4,5,6] Barry McKernan [4,5,6] and Daniel Stern[7]

[1]*Institute for Astronomy, University of Edinburgh, Royal Observatory, Blackford Hill, Edinburgh EH9 3HJ, UK*
[2]*Cahill Center for Astronomy and Astrophysics, California Institute of Technology, Mail Code 249/17, 1200 E California Blvd, Pasadena CA 91125, USA*
[3]*INAF – Osservatorio Astronomico di Trieste, Via Tiepolo 11, I-34143 Trieste, Italy*
[4]*Department of Science, BMCC, City University of New York, New York, NY 10007, USA*
[5]*Department of Astrophysics, Rose Center for Earth and Space, American Museum of Natural History, Central Park West at 79th Street, NY 10024, USA*
[6]*Graduate Center, City University of New York, 365 5th Avenue, New York, NY 10016, USA*
[7]*Jet Propulsion Laboratory, California Institute of Technology, 4800 Oak Grove Drive, Mail Stop 169-221, Pasadena, CA 91109, USA*

Accepted 2020 August 8. Received 2020 July 30; in original form 2020 February 1

ABSTRACT

We report on three redshift $z > 2$ quasars with dramatic changes in their C IV emission lines, the first sample of changing-look quasars (CLQs) at high redshift. This is also the first time the changing-look behaviour has been seen in a high-ionization emission line. SDSS J1205+3422, J1638+2827, and J2228 + 2201 show interesting behaviour in their observed optical light curves, and subsequent spectroscopy shows significant changes in the C IV broad emission line, with both line collapse and emergence being displayed on rest-frame time-scales of ∼240–1640 d. These are rapid changes, especially when considering virial black hole mass estimates of $M_{\rm BH} > 10^9 M_{\odot}$ for all three quasars. Continuum and emission line measurements from the three quasars show changes in the continuum-equivalent width plane with the CLQs seen to be on the edge of the full population distribution, and showing indications of an intrinsic Baldwin effect. We put these observations in context with recent state-change models, and note that even in their observed low-state, the C IV CLQs are generally above ∼5 per cent in Eddington luminosity.

Key words: accretion, accretion discs – surveys – quasars: general – quasars: individual (SDSS J120544.7+342252.4, SDSS J163852.9+28270.7.7, SDSS J222818.7 + 220102.9) – .

1 INTRODUCTION

Luminous AGN, i.e. quasars, are now seen to significantly vary their energy output on time-scales as short as weeks to months. This observation, and the subsequent mismatch in the expected viscous time-scale, which for a $10^7 M_{\odot}$ central supermassive black hole (SMBH) is ∼hundreds of years, was noted over 30 yr ago (e.g. Alloin et al. 1985). However, with new photometric light curve and repeat spectroscopic data, the desire for a deeper understanding of AGN accretion disc physics has recently re-invigorated the field (e.g. Antonucci 2018; Lawrence 2018; Ross et al. 2018; Stern et al. 2018).

The optical continuum variability of quasars was recognized since their first optical identifications (Matthews & Sandage 1963). However, dramatic changes in the broad emission lines (BELs) of quasars was only recently first identified (LaMassa et al. 2015). Samples of over 100 'changing-look' quasars (CLQs) or 'changing-state' quasars (CSQs) have now been assembled (e.g. MacLeod et al. 2019; Graham et al. 2020). The community uses both these terms as a cover for the underlying physics. For sake of argument, CLQs can potentially be thought of as the extension to the BELs of quasar continuum variability (e.g. MacLeod et al. 2012) whereas the CSQs have a state-transition, perhaps similar to that seen in Galactic X-ray binaries (Noda & Done 2018; Ruan et al. 2019). In this paper, we use the term 'changing-look', as we are currently agnostic, and confessedly ignorant, to the underlying physical processes.

CLQs to date have primarily been defined according to the (recombination) Balmer emission line properties with particular attention paid to the H β emission line, observed from optical spectroscopy. Recent works report on discoveries of Mg II changing-look AGN (Guo et al. 2019; Homan et al. 2020). However, current CLQ studies have primarily been at redshifts $z < 1$.

While there have been many studies on triply ionized carbon, i.e. C IV, these have tended to focus on broad absorption line quasars (e.g. table 1 of Hemler et al. 2019) or the Baldwin effect (Baldwin 1977; Bian et al. 2012; Jensen et al. 2016; Hamann et al. 2017). As noted in Rakić et al. (2017), two different types of Baldwin effect are present in the literature: (i) the global (or ensemble) Baldwin effect, which is an anticorrelation between the emission line equivalent width and the underlying continuum luminosity of single-epoch observations of a large number of AGN, and (ii) the intrinsic Baldwin effect, the same anticorrelation but in an individual, variable AGN (Pogge & Peterson 1992). The ensemble and intrinsic Baldwin effect has been observed in the C IV broad absorption line quasar population. However, dramatic changes in the collisionally excited broad emission line of C IV – and indeed C III] – have not to this point been reported.

Here, we present new results for three quasars which show dramatic changes in their C IV and C III] broad emission line properties and underlying continuum. These are some of the first examples of

★ E-mail: npross@roe.ac.uk

Table 1. Strong UV/optical spectral emission lines in quasars, and their atomic data from the NIST Atomic Spectra Data base (Kramida et al. 2018, 2019). The transition energies are $E = hc/\lambda$ for the given wavelength. Transition level configurations are given in standard spectroscopic notation (as Configuration, Term, and quantum J number) with $A_{i,j}$ denoting the transition probabilities. The physical mechanism for the generation of the emission lines, e.g. full ionization, collisional excitation, or recombination, are given in the last column.

Line	λ / Å	Transition Energy / eV	Transition levels Lower; Conf., Term, J			Upper; Conf., Term, J			Wavenumber / cm^{-1}	$A_{i,j}$ / 10^8 s^{-1}	Physical Mechanism
H LyLim	912.324	13.5984	$1s$	^{2}S	1/2	∞			109 678.7	1.23×10^{-6}	Ionization
H Ly α	1215.670	10.1988	$1s$	^{2}S	1/2	2			82 259.2	4.67	Recombination
N V	1238.821	10.0082	$1s^2 2s$	^{2}S	1/2	$1s^2 2p$	^{2}P^o	3/2	80 721.9	3.40	Collisional Ex.
N V	1242.804	9.9762	$1s^2 2s$	^{2}S	1/2	$1s^2 2p$	^{2}P^o	1/2	80 463.2	3.37	Collisional Ex.
C IV	1548.187	8.0083	$1s^2 2s$	^{2}S	1/2	$1s^2 2p$	^{2}P^o	3/2	64 591.7	2.65	Collisional Ex.
C IV	1550.772	7.9950	$1s^2 2s$	^{2}S	1/2	$1s^2 2p$	^{2}P^o	1/2	64 484.0	2.64	Collisional Ex.
He II	1640.474	7.5578	$2p$	^{2}P^o	3/2	$3d$	^{2}D	5/2	60 958.0	10.35	Recombination
He II	1640.490	7.5578	$2p$	^{2}P^o	3/2	$3d$	^{2}D	3/2	60 957.4	1.73	Recombination
He II	1640.533	7.5576	$2p$	^{2}P^o	3/2	$3s$	^{2}S	1/2	60 957.4	0.68	Recombination
C III]	1906.683	6.5026	$1s^2 2s^2$	^{1}S	0	$1s^2 2s 2p$	^{3}P^o	2	52 447.1	5.19×10^{-11}	Collisional Ex.
C III]	1908.734	6.4956	$1s^2 2s^2$	^{1}S	0	$1s^2 2s 2p$	^{3}P^o	1	52 390.8	1.14×10^{-6}	Collisional Ex.
Mg II	2795.528	4.4338	$2p^6 3s$	^{2}S	1/2	$2p^6 3p$	^{2}P^o	3/2	35 760.9	2.60	Collisional Ex.
Mg II	2802.705	4.4224	$2p^6 3s$	^{2}S	1/2	$2p^6 3p$	^{2}P^o	1/2	35 669.3	2.57	Collisional Ex.
H Ba β	4861.333	2.5497	2			4			20 564.8	0.0842	Recombination

CLQs at high ($z > 1$) redshift. Moreover, these are the first cases for substantial changes of ions with high ionization potentials (I.P.'s >2 Rydberg), thus linking the ionizing photons to the energetic inner accretion disc.

Photoionization followed by recombination determines the ionization level of carbon, and collisional excitation from the ions' ground level determines the line intensity. Other processes do happen (including radiative and three-body recombination to the upper levels of the transition), but they are much slower unless the density is extremely high (e.g. Dopita & Sutherland 2003, and H. Netzer, private communication). The ionization potential of C III ion is 47.89 eV (3.519 Ry) and thus a photon with this energy ($k_B T \sim 5.6 \times 10^5$ K) can create the triply ionized, C IV ion. Once the C IV ion is formed, collisional excitation leads to the production of the 1548.202 and 1550.774 Å C IV doublet.

Most of the strong lines in the rest-frame near-UV spectrum of quasars are collisionally excited, including C III] , C IV, and N V. The He II λ1640 recombination line is among the exceptions. Details of the atomic transitions and physical mechanisms that produce strong rest-frame UV/optical lines in quasars are given in Table 1.

Wilhite et al. (2006) examine C IV variability in a sample of 105 quasars observed at multiple epochs by the Sloan Digital Sky Survey (SDSS; York et al. 2000; Stoughton et al. 2002; Abazajian et al. 2009). They find a strong correlation between the change in the C IV line flux and the change in the line width, but no correlations between the change in flux and changes in line centre or skewness. These authors find that the relation between line flux change and line width change is consistent with a model in which a broad-line base varies with greater amplitude than the line core. The C IV lines in these high-luminosity quasars appear to be less responsive to continuum variations than those in lower luminosity AGN.

Richards et al. (2011) explored the broad emission line region in over 30 000 $z > 1.54$ SDSS quasars, concentrating on the properties of the C IV emission line. These authors consider two well-known effects involving the C IV emission line: (i) the anticorrelation between the C IV equivalent width (EW) and luminosity (i.e. the global Baldwin effect) and (ii) the blueshifting of the peak of C IV emission with respect to the systemic redshift. We denote the velocity offset of emission lines as $V_{\rm off}$ and use the convention that a positive $V_{\rm off}$ value means the line is blueshifted while a negative $V_{\rm off}$ value means the line is redshifted. Richards et al. (2011) find a blueshift of the C IV emission line is nearly ubiquitous, with a mean shift of $\langle V_{\rm off} \rangle \sim$810 km s^{-1} for radio-quiet (RQ) quasars and $\langle V_{\rm off} \rangle \sim$360 km s^{-1} for radio-loud (RL) objects. Richards et al. (2011) also find the Baldwin effect is present in both their RQ sample and their RL sample. They conclude that these two C IV parameters (EW and blueshift) are capturing an important trade-off between disc and wind components in the disc–wind model of accretion discs (e.g. Murray et al. 1995; Elvis 2000; Proga, Stone & Kallman 2000; Leighly 2004), with one dominating over the other depending on the shape of the quasar spectral energy distribution (SED).

Using the multi-epoch spectra of 362 quasars from the SDSS Reverberation Mapping project (SDSS-RM; Shen et al. 2015, 2019), Sun et al. (2018) investigate the blueshift of C IV emission relative to Mg II emission, and its dependence on quasar properties. They confirm that high-blueshift sources tend to have low C IV EWs, and that the low-EW sources span a range of blueshift. Other high-ionization lines, such as He II , also show similar blueshift properties. The ratio of the line width of C IV to that of Mg II increases with blueshift. Sun et al. (2018) also find that quasar variability might slightly enhance the connection between the C IV blueshift and EW, though further investigation here is warranted. They also find that quasars with the largest blueshifts are less variable and tend to have higher Eddington ratios, though Eddington ratio alone might be an insufficient condition for the C IV blueshift. Recent investigations also include Meyer, Bosman & Ellis (2019) and Doan et al. (2019). Dyer et al. (2019) provide a detailed analysis of 340 quasars at high redshift ($1.62 < z < 3.30$) from the SDSS-RM project, which we compare with our results in Section 4.2.

The purpose of this paper is, for the first time, to systematically access and report on the CLQ phenomenon at high ($z > 2$) redshift. While accessing this phenomenon at an earlier cosmic epoch is interesting, the main value of this study is to move from the low-ionization energy Balmer emission line series at rest-frame optical wavelengths to the high-ionization emission lines, in particular C IV λ1549, at rest-frame UV wavelengths.

This paper is organized as follows. In Section 2, we describe our sample selection, catalogues, and observational data sets. Section 3 presents the high-redshift quasars and reports their time-variable line properties. We provide a brief theoretical discussion in Section

4, and Section 5 presents our conclusions. We report all magnitudes on the AB zero-point system (Oke & Gunn 1983; Fukugita et al. 1996) unless otherwise stated. For the *WISE* bands, $m_{\rm AB} = m_{\rm Vega} + m$ where $m = 2.699$ and 3.339 for *WISE* W1 (3.4 μm) and W2 (4.6 μm), respectively (Cutri et al. 2011; Cutri 2013). We adopt a flat ΛCDM cosmology with $\Omega_\Lambda = 0.73$, $\Omega_{\rm M} = 0.27$, and $h = 0.71$. All logarithms are to the base 10.

2 CLQ SELECTION AND LINE MEASUREMENTS

A statistical search using optical light curves to initiate spectroscopic follow-up observations is proving an efficient CLQ finder, and, by design, our data sources and overall methodology, are in common to the recent Ross et al. (2018), Stern et al. (2018), and Graham et al. (2020) papers.

In this section, we present the photometric data used to select the CLQs and give details of the multiwavelength data where we have it. We use optical data from the Catalina Real-time Transient Survey (CRTS; Drake et al. 2009; Mahabal et al. 2011), the Panoramic Survey Telescope and Rapid Response System (PanSTARRS; Kaiser et al. 2010; Stubbs et al. 2010; Tonry et al. 2012; Magnier et al. 2013), and the Zwicky Transient Facility (ZTF; Bellm et al. 2019a). We also use data from the *WISE* mission and SDSS. We then give details of the spectroscopic data including emission lines measurements.

2.1 Photometry

2.1.1 Optical Photometry

The CRTS archive[1] contains the Catalina Sky Survey data streams from three telescopes – the 0.7-m Catalina Sky Survey (CSS) Schmidt and 1.5-m Mount Lemmon Survey (MLS) telescopes in Arizona, and the 0.5-m Siding Springs Survey (SSS) Schmidt in Australia. CRTS covers up to ∼2500 deg^2 per night, with four exposures per visit, separated by 10 min. The survey observes over 21 nights per lunation. The data are broadly calibrated to Johnson V (for details, see Drake et al. 2013) and the current CRTS data set contains time series for approximately 400 million sources to $V \sim 20$ above Declination $\delta > -30$ deg from 2003 to 2016 May (observed with CSS and MLS) and 100 million sources to $V \sim 19$ in the Southern sky from 2005 to 2013 (from SSS). CRTS has been extensively used to study quasar variability (e.g. Graham et al. 2014, 2015a, b, 2017, 2020; Stern et al. 2017, 2018; Ross et al. 2018).

PanSTARRS data are obtained via the Pan-STARRS Catalogue Search interface.[2] Specifically, we query the PS1 DR2 Detection catalogue.

ZTF[3] is a robotic time-domain sky survey capable of visiting the entire visible sky north of −30 deg declination every night. ZTF observes the sky in the g, r, and i-bands at different cadences depending on the scientific program and sky region (Bellm et al. 2019b; Graham et al. 2019). The ZTF 576 megapixel camera with a 47 deg^2 field of view, installed on the Samuel Oschin 48-inch Schmidt telescope at Palomar observatory, can scan more than 3750 deg^2 per hour, to a 5σ detection limit of 20.7 mag in the r-band with a 30 s exposure during new moon (Masci et al. 2019).

[1] http://catalinadata.org
[2] https://catalogs.mast.stsci.edu/panstarrs/
[3] http://ztf.caltech.edu) is a new

2.1.2 Mid-infrared photometry

We use mid-infrared data (3.4 and 4.6 μm) from the beginning of the *WISE* mission (2010 January; Wright et al. 2010) through the fifth-year of *NEOWISE-R* operations (2018 December; Mainzer et al. 2011). The *WISE* scan pattern leads to coverage of the full-sky approximately once every six months (a 'sky pass'), albeit it with a gap between 2011 February and 2013 October when the satellite was placed in hibernation. Hence, our light curves have a cadence of 6 months with a 32-month sampling gap.

2.2 CLQ selection

As this is the first time high-redshift CLQs have been studied, defining a formal and automatic process is not an trivial task. Hence we focused on a method and threshold which selects the most promising candidates, with no claim of completeness, for visual inspection.

Our high-redshift CLQs were identified as follows. We selected all 64 774 SDSS DR15 sources with $z > 0.35$ classified as 'quasar', that had at least two spectra separated by ≥100 d, and that had a corresponding CRTS light curve. We fitted a damped random walk to the CRTS data via Gaussian process regression (using the GPy Python library). This allowed us to predict the photometric magnitudes and their uncertainties at the epochs of the SDSS spectra for each source (see Rasmussen & Williams 2006). Candidate objects with $|\Delta V| > 0.3$ magnitude were then selected for visual inspection. This corresponds to at least a 33 per cent change in flux between the two epochs. Approximately 1 per cent of quasars should show this level of variability over the time-scales considered (Graham et al. 2017).

Only three quasars, SDSS J120544.7+342252.4 (hereafter J1205+3422), SDSS J163852.93+282707.7 (hereafter J1638+2827), and SDSS J222818.76+220102.9 (hereafter J2228 + 2201), satisfied these selection criteria and showed interesting or dramatic emission line behaviour.

2.3 Spectroscopy

An overview of our spectroscopic observations is given in Table 2. The archival spectra are from the SDSS (Stoughton et al. 2002; Abazajian et al. 2009; Schneider et al. 2010), the SDSS-III Baryon Oscillation Spectroscopic Survey (BOSS; Eisenstein et al. 2011; Dawson et al. 2013; Smee et al. 2013; Alam et al. 2015; Pâris et al. 2017), and the SDSS-IV Extended Baryon Oscillation Spectroscopic Survey (eBOSS; Dawson et al. 2016; Abolfathi et al. 2018; Pâris et al. 2018). These quasars were targetted via a range of techniques and algorithms (see Richards et al. 2002; Ross et al. 2012; Myers et al. 2015). The SDSS, BOSS, and eBOSS data are supplemented by spectra from the Low Resolution Imaging Spectrometer (LRIS; Oke et al. 1995) on the 10-m Keck I telescope and the Double Spectrograph (DBSP) instrument on the 200-inch Palomar Hale telescope.

Proper comparison of the spectra requires reliable flux calibrations, which is a challenge since not all data were taken in photometric conditions. SDSS spectra are spectrophotometrically calibrated. BOSS and eBOSS spectra have spectrophotometric corrections applied in the latest data release (Hutchinson et al. 2016; Jensen et al. 2016; Margala et al. 2016). However, some of the Palomar and Keck data suffered from variable conditions and clouds. For lower redshift AGN, the narrow [O III] emission line is typically used to align spectrophotometry since it is spatially extended and not expected to change significantly on human time-scales (e.g. Barth et al. 2011). However, due to the high-redshift of our quasars, [O III] is not

Table 2. Details of our spectroscopic observations. Redshift errors are typically ±0.002. SDSS, BOSS, and eBOSS spectra have resolving power $\mathcal{R} \equiv \lambda/\Delta\lambda \sim 2000$. DBSP: Double Spectrograph on the Palomar 200-inch Hale telescope. LRIS: Low Resolution Imaging Spectrometer on Keck I 10-m telescope.

Object	Redshift	g-band / mag	MJD	Instrument	Exposure time s^{-1}	SDSS Plate-FiberID	Notes
	2.068	18.27	53498	SDSS	8057	2089-427	Plate quality marginal
J120544.7+342252.4	2.071	–	58538	DBSP	1800	–	Poor conditions
	2.071	–	58693	DBSP	2400	–	Good conditions
	2.185	19.77	54553	SDSS	4801	2948-614	Plate quality good
J163852.9+282707.7	2.186	–	55832	BOSS	3600	5201-178	Plate quality good
	2.182	–	58583	LRIS	1800	–	–
	2.217	19.97	56189	BOSS	2700	6118-720	Plate quality good
J222818.7+220102.9	2.222	–	56960	eBOSS	4500	7582-790	Plate quality good
	2.222	–	58693	DBSP	2400	–	–

available to us for scaling the spectra. Instead, we use photometric data from ZTF since our Palomar and Keck data were all taken after MJD 57500. This provides broad-band photometry at the time of the spectroscopy, which we use to scale the spectra whose initial calibration is based on spectrophotometric standards observed on the same nights. We estimate the resulting uncertainty in flux calibration is ∼5 per cent. This uncertainty is not propagated into measurements.

2.4 Emission line and power-law slope measurements

We use the measured quasar emission line properties from several catalogues: Shen et al. (2011), Hamann et al. (2017), Kozłowski (2017), and Calderone et al. (2017).

In particular, we use the Quasar Spectral Fitting (QSFIT) software package presented in Calderone et al. (2017). This provides luminosity estimates as well as width, velocity offset, and EWs of 20 emission lines, including C IV, C III], and Mg II. We process and fit all nine spectra (3 quasars with 3 epochs) using the lastest version (v1.3.0) of the QSFIT online calculator. The host galaxy and blended iron emission at rest-frame optical wavelengths components are automatically disabled when they cannot be constrained by the available data, as is the case for all our quasars. Power-law continuum slopes, α, where $f_\lambda \propto \lambda^\alpha$, are also reported in these catalogues and from QSFIT.

As described in Calderone et al. (2017), the uncertainties in the measured quantities are determined by two methods: a Fisher matrix method and a Monte Carlo resampling method. One might expect correlations among model parameters, e.g. emission-line luminosities and widths, potentially causing the Fisher matrix method to underestimate the errors. However, upon investigation, the parameters of the involved model components (a power-law for the continuum and a single Lorentzian profile for the emission lines) show negligible correlations. Therefore, we use the Fisher matrix method to estimate the uncertainties on the model parameters.

3 RESULTS

3.1 Photometric and overall spectral evolution

Fig. 1 presents the optical and mid-infrared light curves for three high-redshift CLQ quasars. Fig. 2 shows the rest-frame spectra for SDSS J1205+3422. For J1205+3422, our spectral observations cover 5195 observed days, corresponding to 1691d in the rest-frame. This quasar was initially identified in SDSS in 2005 May as a bright, $g \approx 18.0$, blue-sloped quasar with broad Si IV/O IV, C IV, C III], and Mg II emission. C IV has a blueshift of ≈580 ± 80 km s^{-1}. By 2019, however, the optical brightness dropped by nearly 2 magnitudes and the spectra are significantly less blue. Ly α and N V are detectable in both 2019 spectra, but is just bluewards of the wavelength range covered by the original SDSS spectrum. The C IV and C III] lines have faded significantly between the SDSS observation in 2005 and the Palomar observations in 2019. Note that C IV is extremely faint in the 2019 February spectrum (MJD 58538), but that night suffered from poor conditions.

Fig. 3 shows the rest-frame spectra for SDSS J1638+2827. For J1638+2827, our spectral observations cover 4030 observed days, corresponding to 1265 d in the rest-frame. Here, in the initial epoch spectrum, C IV is broad and bright, as is C III]. However, ≈400 rest-frame days later, the broad C IV and C III] emission lines have faded, the continuum slope around 1400 Å has changed from ≈−1.16 to ≈−2.17, but the Ly α /N V emission complex is very similar in shape and intensity. Around 870 d in the rest-frame after the second spectral epoch, at the time of the third spectral epoch, the source has brightened from optical magnitudes of ∼20 mag to ∼18.5 mag. Ly α, N V, C IV, C III] , and Mg II are all apparent and broad, with Mg II being seen for the first time at high signal-to-noise. An absorption feature between Ly α and N V is seen in all three spectral epochs.

Fig. 4 shows the rest-frame spectra for SDSS J2228+2201. For J2228+2201, our spectral observations cover 2504 observed days, corresponding to 778 d in the rest-frame. Over the course of 240 rest-frame days, C IV and C III] both emerge as BELs and the standard UV/blue continuum becomes stronger. Then, over the course of 538 d in the rest-frame, the broad emission, while still very present, reduces in line flux and the UV/blue continuum diminishes. However, the third epoch still corresponds to a source more luminous than the initial BOSS spectrum.

3.2 C IV emission line evolution

We analyse the multi-epoch spectra of the three quasars using the QSFIT spectral fitting package (Calderone et al. 2017). One advantage of using QSFIT is that it allows constraints on the slope and luminosity of the broad-band continuum of the source. The relevant estimated quantities, including continuum luminosity and slope at rest-frame 1450 Å, C IV line luminosity, full width at half-maximum (FWHM), and EW are given in Table 3. All fits are obtained by taking the Milky Way extinction (Schlafly & Finkbeiner 2011) into account. The extinction values are: $E(B-V) = 0.013$ for J1205+3422; $E(B-V) = 0.034$ for J1638+2827, and $E(B-V) = 0.041$ for J2228+2201, as taken from the NASA/IPAC Extragalactic Database. The best-fitting models in the region of the C IV emission line are shown in Fig. 5.

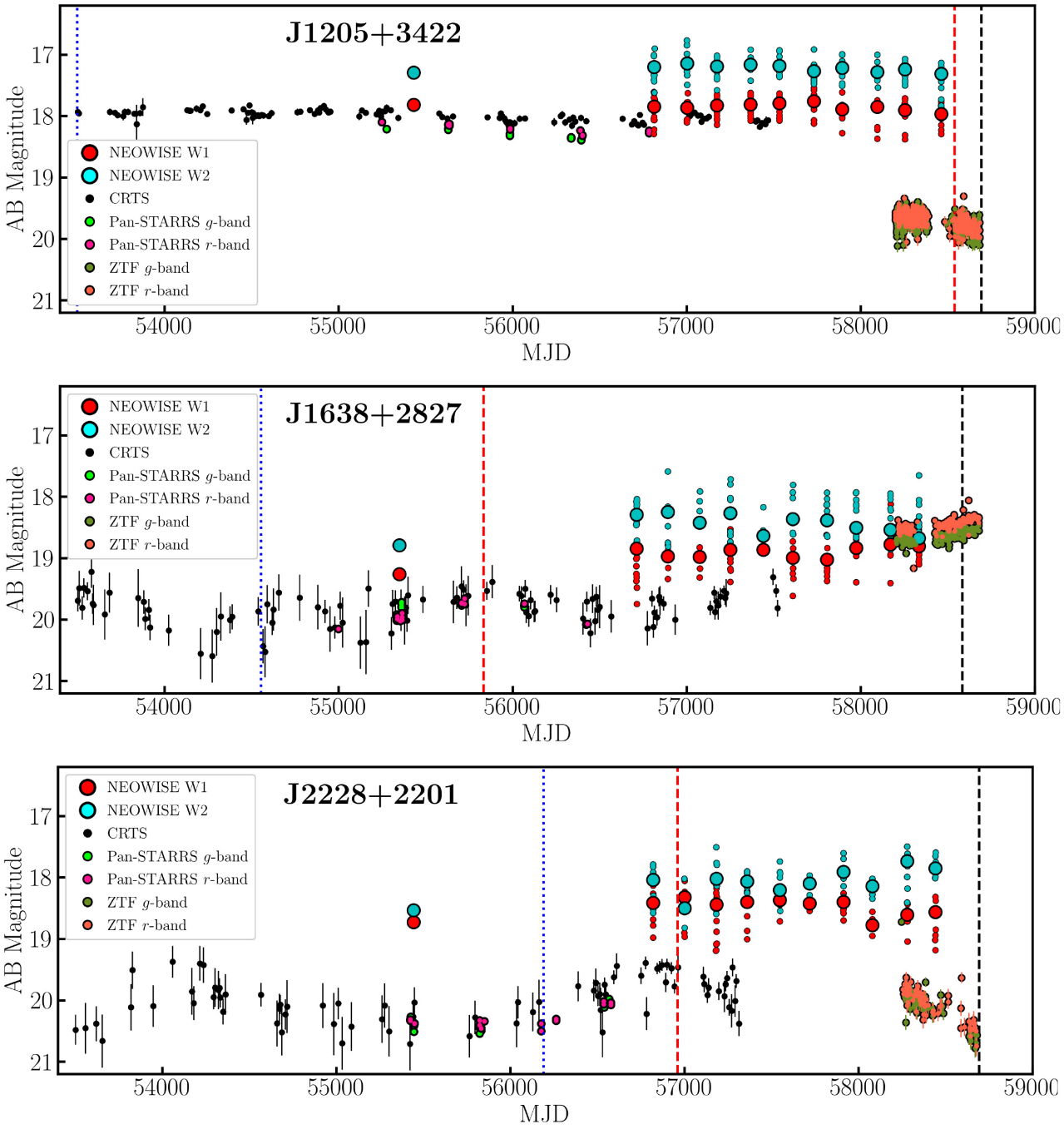

Figure 1. The light curves for the three high-redshift CLQ quasars; J1205+3422 (top), J1638+2827 (middle), and J2228+2201 (bottom). The timing of the spectral observations are indicated with vertical dashed lines.

All C IV lines are fitted with a single, broad, Lorentzian profile. This allows us to account for the central peak of the C IV line. After experimenting, we decided not to include additional narrow components for several reasons. First, in the epochs of highest brightness, such a 'narrow' component would have FWHM $\sim$ 2000–3000 km s^{-1}, i.e. values exceeding the usual widths of genuine narrow lines ($\lesssim$1000 km s^{-1}). Secondly, allowing a second component to have such large widths would make that component highly degenerate with the 'broad' components, causing the latter to have much larger widths, $\sim$10 000 km s^{-1}. Finally, neglecting such a narrow component ensures a consistent model across all epochs.

Both the quasar continuum (evaluated at 1450 Å) and the C IV line luminosities follow a similar evolution, with a ratio of $\sim$20–30, confirming that the main driver for emission line variability is likely the broad-band continuum itself. For all sources except J1638+2827, the slope of the continuum changes with luminosity following a 'bluer-when-brighter' pattern, suggesting that a distinct emerging component is responsible for both the slope and luminosity variations. In J1638+2827 the opposite behaviour is observed, especially in the first observation epoch. However, this may be a bias due to the limited wavelength range available which extends to rest-frame λ $\sim$1240 Å for the first epoch, while it extends to

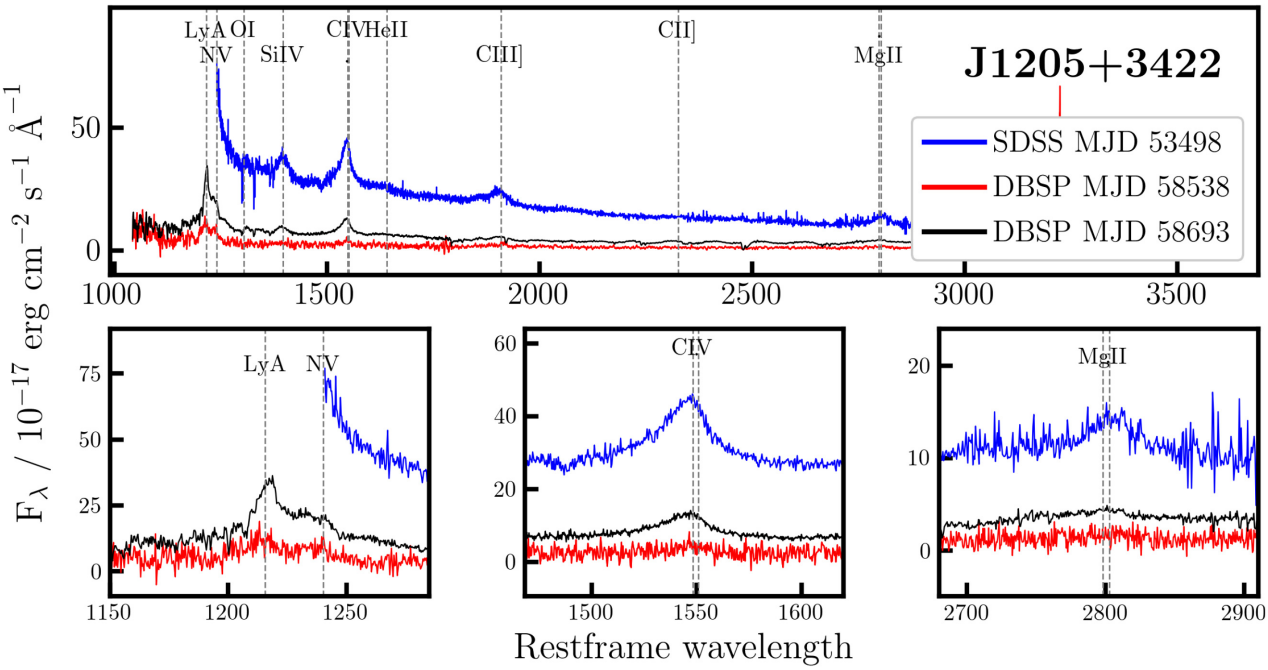

Figure 2. The three epochs of spectra for SDSS J1205+3422. The full wavelength spectrum is presented in the top panel, with zoom-in's on the Ly α-N V complex, the C IV line, and the Mg II line in the lower panels.

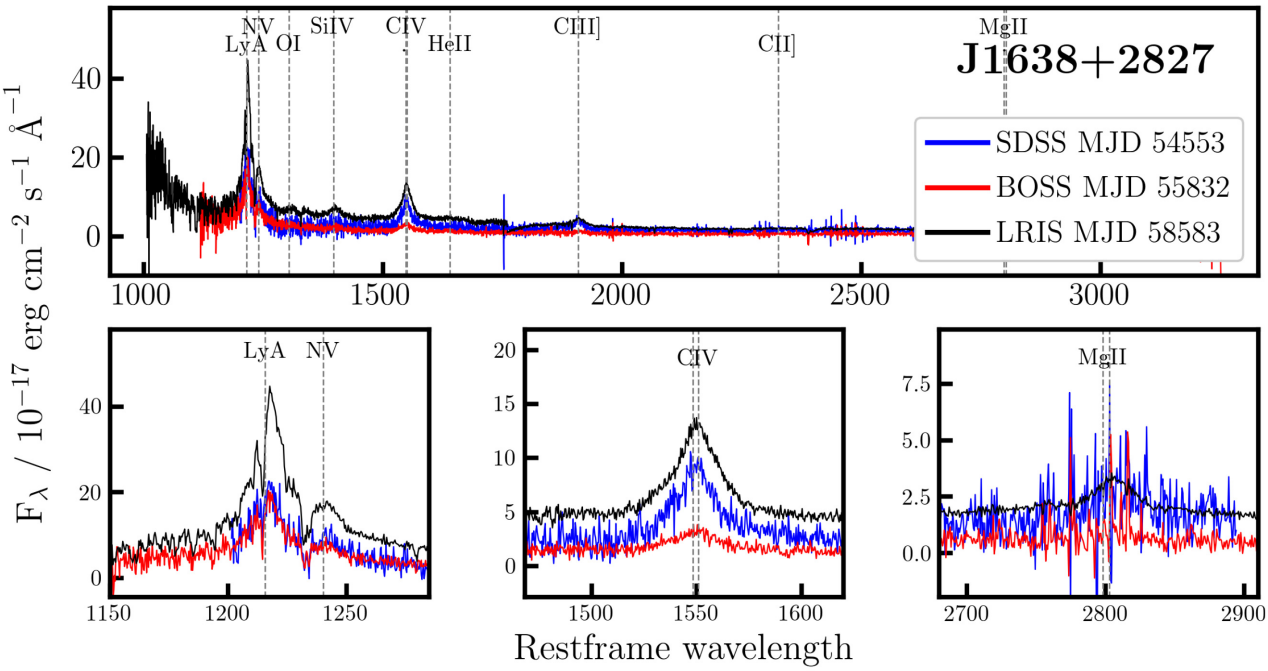

Figure 3. As Fig. 2 but for J1638+2827.

shorter wavelengths for the other epochs (respectively 1100 and 1010 Å). This is consistent with the emerging component being more prominent at UV wavelengths, and suggests a sufficient wavelength coverage is required to detect it. In all cases where the C IV line profile is reliably constrained, we find that the C IV FWHM is approximately constant with maximal variations $\lesssim$1000 km s^{-1}, despite significantly larger line luminosity variations.

3.3 Virial black hole masses

The FWHMs of quasar broad lines are related to the mass of the SMBH powering the quasar phenomenon, and that mass is assumed to be constant on any human time-scale. Hence it is instructive to check whether the virial products, which are the basic quantity used to calculate single-epoch black hole mass estimates, show any variation. The continuum luminosity provides a proxy for the BLR radius, and

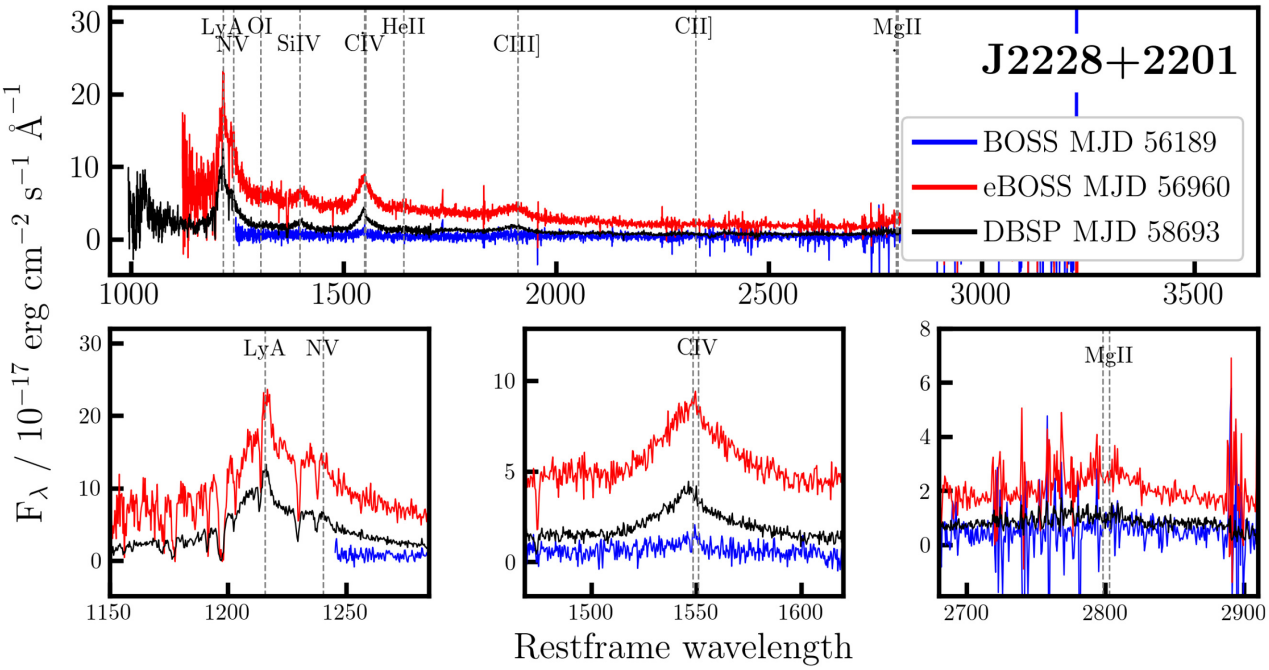

Figure 4. As Fig. 2 but for J2228+2201.

Table 3. Continuum at 1450 Å and C IV spectral measurements for the three quasar considered in this work, at all observation epochs, as calculated by QSFIT. For the emission-line velocity offsets, a positive value means the line is blueshifted. The last column shows the virial product calculated as $(\nu L_\nu)^{0.5} \times \mathrm{FWHM}^2$. The last column shows the virial product calculated as $(\nu L_\nu)^{0.5} \times \mathrm{FWHM}^2$, and its uncertainty (calculated by propagating uncertainties on both νL_ν and the FWHM). The virial products are calculated to check if the BH mass varies significantly across epoch. *The C IV line is very faint (with respect to the continuum), and the associated estimates are likely unreliable.

Object	MJD	Cont. @ 1450Å νL_ν /10^{42} erg s^{-1}	Slope ($F_\lambda \propto \lambda^\alpha$)	CIV 1549Å Luminosity /10^{42} erg s^{-1}	FWHM / km s^{-1}	V_{off} / km s^{-1}	EW / Å	Virial product $\log(\nu L_\nu)^{0.5} \times \mathrm{FWHM}^2$
	53498	41630 ± 40	−1.70 ± 0.01	700 ± 49	4700 ± 120	580 ± 80	27 ± 1	9.66 ± 0.02
J1205 + 3422	58538*	2870 ± 40	−1.29 ± 0.09	170 ± 30	14900 ± 2800	980 ± 690	92 ± 16	10.08 ± 0.14
	58693	9050 ± 10	−1.46 ± 0.00	400 ± 5	6980 ± 90	1080 ± 30	70 ± 1	9.67 ± 0.01
	54553	4060 ± 120	−1.4 ± 0.2	330 ± 10	4630 ± 190	180 ± 60	128 ± 4.4	9.14 ± 0.04
J1638 + 2827	55832	2570 ± 20	−2.16 ± 0.06	100 ± 5	4990 ± 300	190 ± 90	64 ± 3.2	9.10 ± 0.05
	58583	8600 ± 20	−2.01 ± 0.01	420 ± 5	4620 ± 70	100 ± 20	81 ± 0.93	9.30 ± 0.01
	56189*	860 ± 40	−0.6 ± 0.1	40 ± 10	5930 ± 990	450 ± 290	73 ± 9.8	9.01 ± 0.13
J2228 + 2201	56960	9150 ± 30	−1.88 ± 0.02	340 ± 10	7000 ± 200	-255 ± 60	60 ± 1.4	9.67 ± 0.03
	58693	2810 ± 5	−1.38 ± 0.01	160 ± 5	5930 ± 80	180 ± 30	91 ± 0.95	9.27 ± 0.01

the broad-line width (FWHM) provides a proxy for the virial velocity. This approach assumes that the broad-line region (BLR) is virialized (e.g. Shen et al. 2008, 2011; Calderone et al. 2017; Mejía-Restrepo et al. 2018) and the virial mass estimate is then:

$$\log\left(\frac{M_{\rm BH}}{M_\odot}\right) = a + \log\left[\left(\frac{L_{1450}}{10^{44}\ \mathrm{erg\ s^{-1}}}\right)^{\gamma}\right] + 2\log\left(\frac{\mathrm{FWHM}}{\mathrm{km\ s^{-1}}}\right), \quad (1)$$

where L_{1450} is the monochromatic continuum luminosity at 1450 Å and FWHM is the full width at half-maximum of the broad C IV emission line. The coefficient γ and offset a are generally determined empirically.

The C IV line is observed to have line asymmetry due to outflows (e.g. Gaskell 1982), very strong blueshifts (as mentioned in the Introduction; see Richards et al. 2011), and a component of the line profile that does not reverberate (Denney 2012). These issues make the C IV virial BH mass estimate uncertain. Runnoe et al. (2013), Mejía-Restrepo et al. (2016), Coatman et al. (2017), Mejía-Restrepo et al. (2018), and Grier et al. (2019) all present studies into improving C IV-based single-epoch black hole mass estimates. With these caveats in mind, we acknowledge the BH mass estimates will have a large error, likely ∼0.5 dex.

We report the virial product for the C IV CLQs in the last column of Table 3. Since our purpose is to check if this measurement varies significantly across epochs, here we use $\gamma = 0.5$ as the power-law slope and are not directly concerned with the offset. The quoted uncertainties account only for the propagation of uncertainties in the continuum luminosities and line widths. As noted above, with typical uncertainties associated to single epoch virial mass around ∼0.5 dex, this implies that the virial products for our three high-redshift CLQs are all remarkably constant and compatible with single black hole masses per source, even in those cases where the C IV estimates

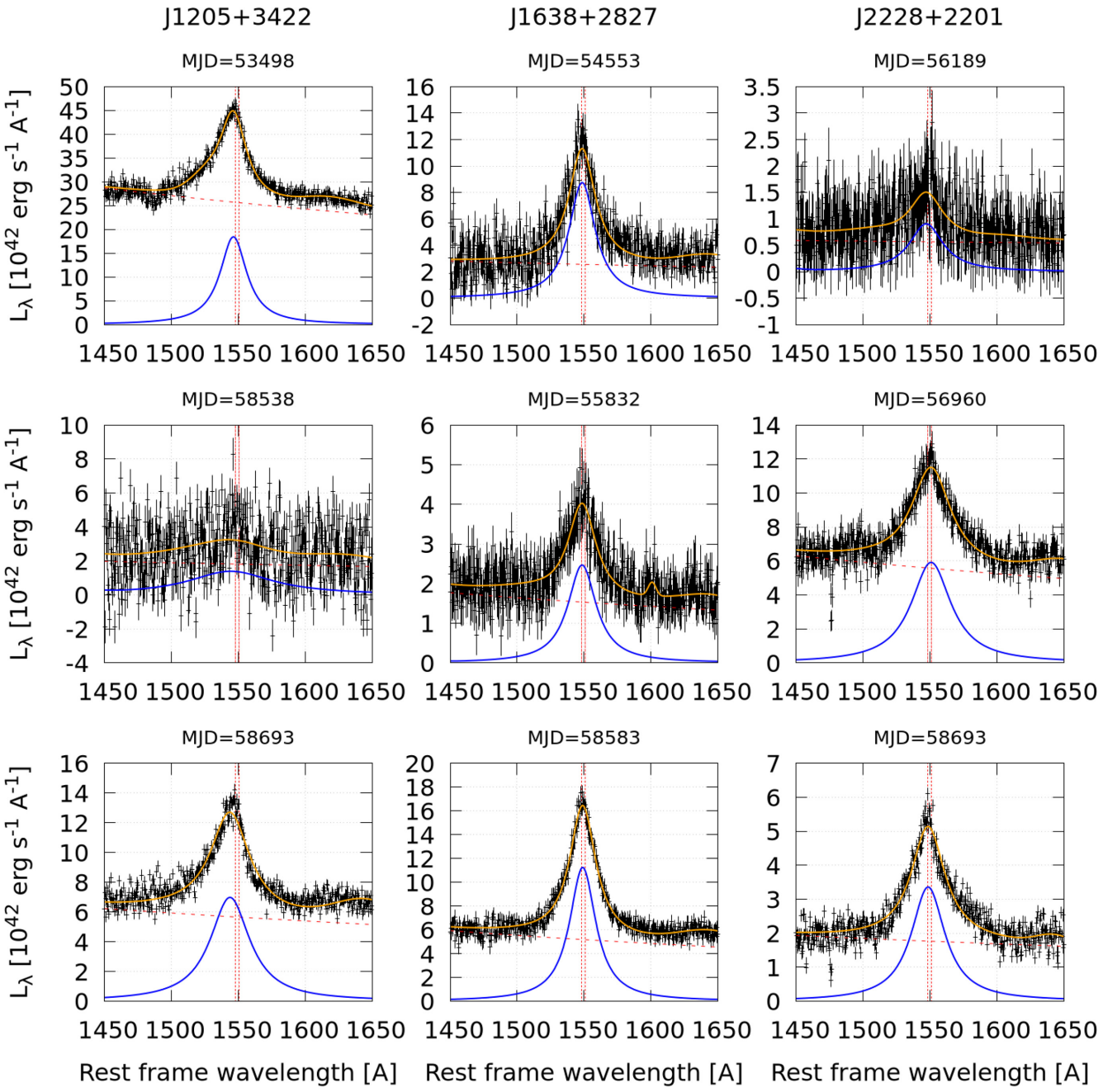

Figure 5. Observed spectra and best-fitting models of the C IV spectral region. The solid blue line is the Lorentzian profile fit to the C IV emission line. The long-dashed red line is the continuum fit, with the solid orange line giving the overall fit. The short-dashed vertical lines give the rest wavelengths of the C IV doublet.

were deemed potentially unreliable. The object showing the largest variation is J2228+2201, with the BH mass estimate spanning a range of 0.66 dex.

For equation (1), Vestergaard & Peterson (2006) measure $\gamma = 0.53$ and the offset as $a = 0.660$, and these estimates are widely adopted (e.g. Shen et al. 2011; Chen et al. 2019; Yao et al. 2019). Kozłowski (2017) have similar values to Vestergaard & Peterson (2006) , with $(a, \gamma) = (0.64, 0.53)$, but note that there is a problem with the C IV FWHMs for those quasars that are reported in both the DR7 Quasar catalogue and DR12 Quasar catalogue. Grier et al. (2019) measure a slope of $\gamma = 0.51 \pm 0.05$ for their sample of high-redshift ($z > 1.3$) quasars that show significant lag measurements, and $\gamma = 0.52 \pm 0.04$ for their 'gold sample' of 16 of their highest-confidence objects.

In Table 4 we report the C IV virial masses calculated using the measured luminosites and FWHM from QSFIT, equation (1) and the Vestergaard & Peterson (2006) calibrations. Shen et al. (2011) and Kozłowski (2017) report virial black hole masses based on Mg II and C IV for the SDSS/BOSS observations of our targets. For J1205+3422 (and MJD 53498), Shen et al. (2011) report $\log(M_{\rm BH,\,MgII}/M_\odot) = 9.55 \pm 0.05$ and $\log(M_{\rm BH,\,CIV}/M_\odot) = 9.49 \pm 0.04$, while for J1638+2827 (MJD 54553), Shen et al. (2011) report $\log(M_{\rm BH,\,MgII}/M_\odot) = 9.03 \pm 0.37$ and $\log(M_{\rm BH,\,CIV}/M_\odot) =$

Table 4. The C IV virial mass estimates, bolometric luminosities, and Eddington ratios for the three quasars. The virial masses are calculated using the measured 1450 Å monochromatic luminosites and C IV FWHM as reported by QSFIT, with * designating the low SNR line measurements. † designates values from the Shen et al. (2011) SDSS DR7 Quasar catalogue. ‡ designates values from the Kozłowski (2017) SDSS-III BOSS DR12 quasar catalogue. The Eddington luminosity is $L_{\rm Edd} = 1.26 \times 10^{38} (M_{\rm BH}/M_{\odot})$ erg s^{-1} and $\eta_{\rm Edd}$ is the log of the Eddington ratio.

Object	MJD	log $(M/M_{\odot})$	log$(L_{\rm bol})$	$\eta_{\rm Edd}$
J1205+3422	53498	9.49†	47.22†	− 0.38†
	53498	9.39	47.20	− 0.29
	*58538	9.78	46.03	− 1.84
	58693	9.38	46.54	− 0.95
J1638+2827	54553	8.74†	46.17†	− 0.68†
	54553	8.84	46.19	− 0.75
	55832	9.13‡	46.72	− 0.72‡
	55832	8.80	45.99	− 0.91
	58583	9.01	46.52	− 0.60
J2228+2201	56189	8.73‡	46.23‡	− 1.32‡
	56189	8.70	45.51	− 1.29
	56960	9.39	46.54	− 0.95
	58693	8.97	46.03	− 1.05

8.74 ± 0.15. These are all within ≈0.1–0.6 dex of the values we calculated for these epochs.

The values in Table 3 are ≈0.3 dex higher than the estimates in Table 4, which is to be expected given the difference of calibrations factors. In fact, the virial products are all remarkably constant and compatible with a single black hole mass estimate, within the standard 0.5 dex uncertainty, across the three epochs for all the quasars.

From the virial mass estimates, all our objects have SMBH masses $M_{\rm BH} \approx 5$–$60 \times 10^8 M_{\odot}$. This is at the upper end of SMBH masses at all epochs, and towards the extreme of the mass distribution for $z \sim 2$ quasars. Fig. 6 compares the luminosity C IV EW versus the virial SMBH masses for our multi-epoch observations to a sample of ≈20 000 $z > 1.5$ SDSS quasars from the QSFIT catalogue (Calderone et al. 2017).

With the black hole masses in hand, we can calculate the Eddington luminosities of the three quasars. To be consistent with the bolometric luminosity, $L_{\rm bol}$, reported in Shen et al. (2011) and Kozłowski (2017) use the bolometric corrections of $\rm BC_{1350} = 3.81$ (from the composite spectral energy distribution in Richards et al. 2006) and to be consistent with those measurements we adopt the same correction. We report the the bolometric luminosities and the Eddington ratios, $\eta = \log (L/L_{\rm Edd})$, in Table 4.

3.4 Quantified temporal evolution of C IV emission

Quasars with interesting physical properties, such as extreme outflows, can be selected using EW and FWHM measurements (e.g. 'Extremely Red Quasars' – Ross et al. 2015; Zakamska et al. 2016, 2019; Hamann et al. 2017). Fig. 7 shows the rest-frame EW versus the FWHM of the C IV emission line in the BOSS DR12 quasar sample from the catalogue of Hamann et al. (2017). Other than the low quality, suspect observation, the multi-epoch observations of our high-redshift CLQs are all consistent with the bulk of the BOSS DR12 sample.

The temporal evolution of the velocity offsets, 1450 Å continuum luminosity, continuum slope, C IV line width (FWHM), and virial black hole mass estimates are shown in Fig. 8. The C IV velocity

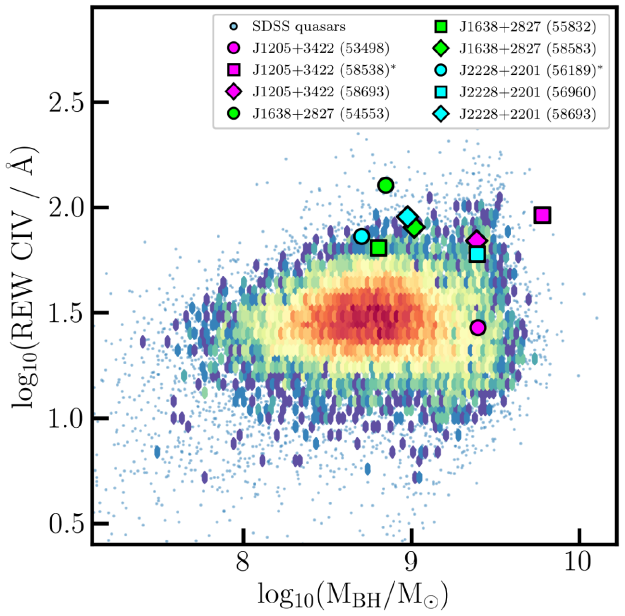

Figure 6. Virial black hole masses of ≈20 000 $z > 1.5$ quasars from the QSFIT catalogue (Calderone et al. 2017) compared to their C IV rest-frame equivalent widths (REWs). Overplotted are the three high-redshift CLQs considered here: J1205+3422 (magenta), J1638+2827 (green), and J2228+2201 (cyan). The symbol shapes indicate the observation epoch, with the first, second, and third epochs denoted by circles, squares, and diamonds, respectively. As per Table 3, an asterisk in the inset box signifies that the C IV line for that quasar observation is very weak, likely making the associated estimates unreliable.

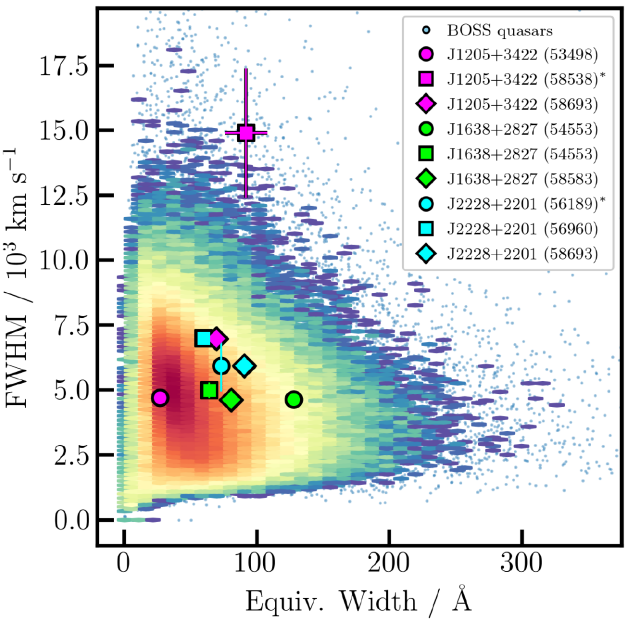

Figure 7. Rest-frame EW versus FWHM of C IV for BOSS DR12 quasar sample (Hamann et al. 2017). Symbols as in Fig. 6.

offsets are approximately constant, and generally compatible with a single value (within 3σ). The exception is J2228+2201, where a significant change ($\sim 7\sigma$) is observed between the second and third epochs. The velocity blueshifts (∼200–1100 km s^{-1}) are consistent with rest-frame UV spectra of quasars over the redshift range $1.5 \leq z \leq 7.5$ (e.g. Meyer et al. 2019).

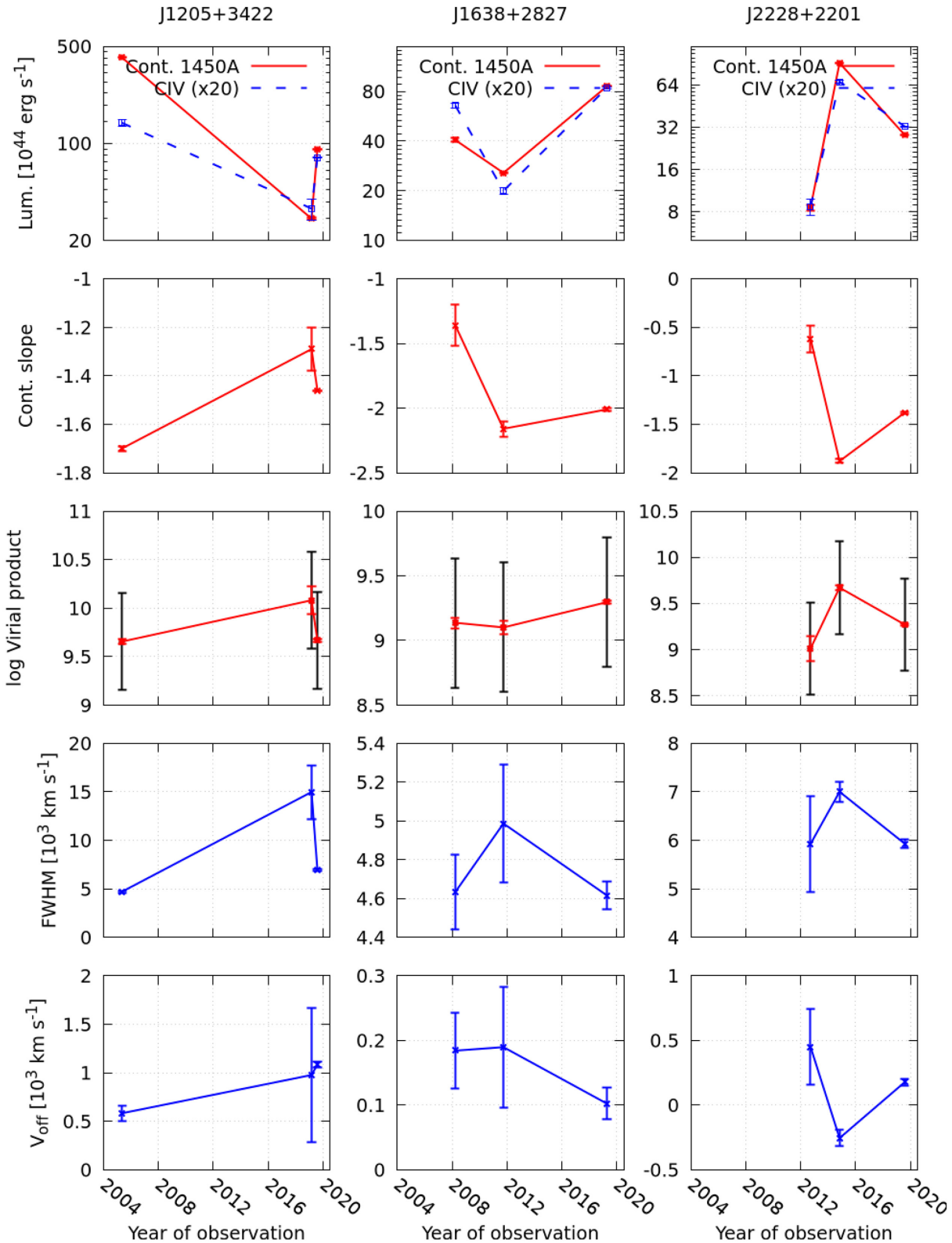

Figure 8. Temporal evolution of the spectral properties of the three quasars considered in this work (see Table 3). The third row show the logarithmic virial product with two error bars: the propagated uncertainties for the $(\nu L_\nu)^{0.5} \times \mathrm{FWHM}^2$ estimates (red) and the typical uncertainty associated to single epoch virial masses (0.5 dex, black).

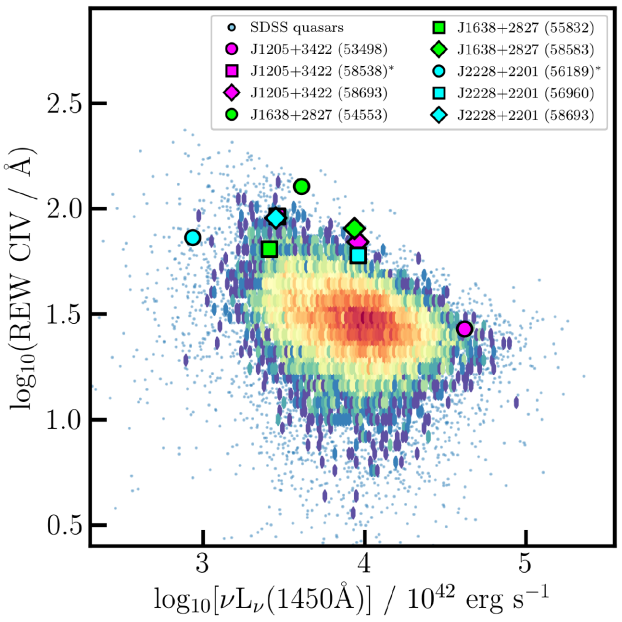

Figure 9. C IV (rest-frame) equivalent width versus underlying continuum luminosity, commonly referred to as the Baldwin plot. The continuum luminosities are from Calderone et al. (2017). The rest-frame EW (REW) measurements are from Table 3. Symbols as in Fig. 6.

3.5 The C IV Baldwin effect

The Baldwin effect (Baldwin 1977) is an empirical relation between quasar emission line rest-frame EWs and continuum luminosity (e.g. Shields 2007; Calderone et al. 2017; Hamann et al. 2017). Hamann et al. (2017) and Calderone et al. (2017) present recent measurements of the Baldwin effect for large quasar samples.

There is an anticorrelation between the rest-frame EWs and, e.g. 1450 Å rest-frame continuum luminosity, so that as the underlying UV continuum luminosity increases, the EW decreases. Fig. 9 shows this for a sample of 20 374 quasars from the QSFIT catalogue (Calderone et al. 2017). The slope is $\beta = -0.20$, consistent with Kozłowski (2017, $\beta = -0.25$, but for bolometric luminosity rather than rest-frame UV continuum luminosity) and with Hamann et al. (2017, $\beta = -0.23$).

We add the measurements from the three C IV CLQs at each epoch to Fig. 9. All three quasars at all three epochs lie on the edge of the νL_ν–EW distribution. Also, with the exception of J1638+2827 on MJD 55832, all the measurements show an intrinsic Baldwin effect (e.g. Goad, Korista & Knigge 2004; Rakić et al. 2017).

4 DISCUSSION

4.1 Continuum and line changes: comparisons to recent observations

The top row of Fig. 8 demonstrates that both the 1450 Å continuum and the C IV emission lines can exhibit large, greater than an order-of-magnitude, changes in luminosity, and that these continuum-line changes track each other.

Trakhtenbrot et al. (2019) report on the quasar 1ES 1927+654 at $z = 0.02$, which was initially seen to lack broad emission lines, i.e. it was a 'type 2' quasar. This object was then seen to spectroscopically change with the appearance of a blue, featureless continuum, followed by the emergence of broad Balmer emission lines – i.e. this quasar changed into a broad-line, or 'type 1' quasar, after the continuum luminosity brightened. This implies that there is (at least in some cases) a direct relationship between the continuum and broad emission lines in CLQs. Many other examples of a similar phenomenon have been reported, albeit not with the dense spectral cadencing of 1ES 1927+654. A similar scenario may have occurred for the three high-redshift CLQs presented here, although we lack the high-cadence, multiwavelength, multi-epoch coverage that Trakhtenbrot et al. (2019) present. Interestingly, Trakhtenbrot et al. (2019) find no evidence for broad UV emission lines in their source, including neither C IV, C III], nor Mg II . The authors attribute the lack of broad UV emission lines to dust within the BLR.

MacLeod et al. (2019) present a sample of CLQs where the primary selection requires large amplitude ($|\Delta g| > 1$ mag, $|\Delta r| > 0.5$ mag) variability over any of the available time baselines probed by the SDSS and Pan-STARRS1 surveys. They find 17 new CLQs, corresponding to ∼20 per cent of their observed sample. This CLQ fraction increases from 10 per cent to roughly half, as the rest-frame 3420 Å continuum flux ratio between repeat spectra increases from 1.5 to 6 – i.e. more variable quasars are more likely to exhibit large changes in their broad emission lines. MacLeod et al. (2019) note that their CLQs have lower Eddington ratios relative to the overall quasar population.

Using the same data set as MacLeod et al. (2019), Homan et al. (2020) investigate the responsiveness of the Mg II broad emission line doublet in AGN on time-scales of several years. Again focussing on quasars that show large changes in their optical light curves, Homan et al. (2020) find that Mg II clearly does respond to the continuum. However, a key finding from Homan et al. (2020) is that the degree of responsivity varies strikingly from one object to another. There are cases of Mg II changing by as much as the continuum, more than the continuum, or very little at all. In the majority (72 per cent) of this highly variable sample, the behaviour of Mg II corresponds with that of H β. However, there are also examples of Mg II showing variations while H β does not, and vice versa.

Graham et al. (2020) report the largest number of H β CLQs to date, with a sample of 111 sources identified. Graham et al. (2020) find that this population of extreme varying quasars, referred to as CSQs in their paper, is associated with changes in the Eddington ratio rather than simply the magnitude of the Eddington ratio itself. They also find that the time-scales imply cooling/heating fronts propagating through the disc.

4.2 Continuum and line changes: comparisons to theoretical expectations

The C IV line is one of the strongest collisionally excited lines in quasar spectra (e.g. Hamann & Ferland 1999). Early measurements from e.g. Pogge & Peterson (1992) and Peterson (1997), using the well-studied Seyfert galaxy NGC 5548, suggested the location of C IV emission was produced by the innermost disc, with the line emission responding to the underlying continuum emission in only a matter of ∼8 d, as indicated by reverberation mapping time-delay measurements. NGC 5548 has an SMBH mass of $\sim 70 \times 10^6 M_\odot$ (Horne et al. 2020) and the bolometric luminosity of NGC 5548 is between ∼0.2 and 10 per cent of the Eddington luminosity (Ebrero et al. 2016; Fausnaugh et al. 2016), giving a log ($L_{\rm bol,\ NGC5448}$/ erg s^{-1}) = ∼43.2–44.9. Thus, the CIV CLQs have a central SMBH mass of ∼7–90× that of NGC 5548, and a bolometric luminosity ∼3–1400× greater. Quasars in the recent Grier et al. (2019) study are of comparable redshift and luminosity to J1205+3422, J1638+2827, and J2228+2201. Grier et al. (2019) measure the lag between the C IV line and the continuum to be of the order of >100 observed-frame days.

In standard Shakura & Sunyaev (1973) thin disc models, large changes in the continuum flux are not permitted over short time-scales due to the relatively long viscous time associated with such discs. Given the observed short time-scale continuum variations, we must consider more complex models. We note that one of our sources (J1205+3422) has C IV EW and continuum luminosity changes which fall comfortably along a line, implying their variation is consistent with an intrinsic Baldwin effect (see Fig. 9). The light-crossing time of the region that produces the C IV line is substantial, which translates into a delay between the variations of the continuum and the C IV line, and a smoothing of the light curve of the latter. Thus, if the excitation of the C IV line is driven by the changes in the continuum, the excited gas cannot reach an equilibrium excitation state as quickly as the continuum changes. This makes the slope of the intrinsic Baldwin effect greater than that of the overall ensemble slope, which is derived from many single-epoch observations, the majority of which are assumed to be in equilibrium.

The presence of an intrinsic Baldwin effect implies those sources may comfortably fit into the sample of C IV variable quasars explored by Dyer et al. (2019). Similar to those authors, we consider slim accretion disc models (e.g. Abramowicz et al. 1988), which may explain the observed variability. In particular, the summary of disc variation time-scales presented in Stern et al. (2018) shows that time-scales are shorter for taller discs, permitting changes similar to those observed if they are caused by heating or cooling fronts propagating on the disc sound crossing time. Dyer et al. (2019) also consider inhomogeneous disc models (e.g. Dexter & Agol 2011) where flux variations are driven by azimuthal inhomogeneities in the temperature of the disc. Such inhomogeneities could arise from disc instabilities (e.g. Lightman & Eardley 1974) or interactions of embedded objects (e.g. McKernan et al. 2014, 2018). If an inhomogeneous disc is responsible for the continuum variations, which then drive C IV variations, it implies that J1205+3422 is simply an extreme outlier produced by a process which occasionally, but rarely, produces very large hot or cool spots. The frequency of such occurrences can be used to constrain the slope and normalization of the power-law distribution of spot size.

Finally, we must also consider the disc/wind model which has successfully reproduced many features of quasar C IV observations, notably the common blueshifted offset (e.g. Murray et al. 1995). In this model, C IV is optically thick at low velocities, but optically thin at high velocities, with $\tau \sim 1$ at $\sim$5000 km s^{-1}. In a disc/wind model, the BLR is very small, implying short time-scales of emission line variability. Also in this model, there should be associated strong absorption in the soft X-ray band, which could be tested with follow-up observations.

The foregoing discussion directly applies to J1205+3422, which maintains a clear intrinsic Baldwin effect relationship between C IV EW and continuum luminosity (J2228+2201 may also be consistent with this picture, given the measurement uncertainties). However, J1638+2827 clearly does not maintain such a relationship – indeed, the continuum and C IV EW appear somewhat correlated, rather than anticorrelated, in this source. This implies that the illumination of the C IV emitting region by a variable ionizing continuum and the corresponding change in the photoionization state alone cannot explain the collapse and recovery of the line.

4.3 Eddington ratios and state changes

The broad UV and optical lines in quasars are most sensitive to the extreme ultraviolet (EUV) part of the SED, with C IV (and indeed He II and N V) being at the higher energy end of the EUV distribution.

Noda & Done (2018) note that the soft X-ray excess – the excess of X-rays below 2 keV with respect to the extrapolation of the hard X-ray spectral continuum model, and a common feature among Type 1 AGN – produces most of the ionizing photons, so its dramatic drop can lead to the disappearance of the broad-line region, driving the changing-look phenomena. Noda & Done (2018) go on to make a connection between state changes in Galactic binaries and CLQs. In Galactic binaries, spectral hardening corresponds to the soft-to-hard state transition in black hole binaries, which occurs at $L/L_{\rm Edd} \sim 0.02$ (i.e. $\eta_{\rm Edd} \sim -1.7$). During this state transition, the inner disc evaporates into an advection-dominated accretion flow, while the overall drop in luminosity appears consistent with the hydrogen ionization disc instability. Noda & Done (2018) predict that changing-look AGNs are similarly associated with state transitions at $L/L_{\rm Edd}$ of a few per cent.

Comparing observed correlations between the optical-to-X-ray spectral index (i.e. $\alpha_{\rm ox}$) and Eddington ratio in AGN to those predicted from observations of X-ray binary outbursts, Ruan et al. (2019) find a remarkable similarity to accretion state transitions in prototypical X-ray binary outbursts, including an inversion of this correlation at a critical Eddington ratio of $\sim 10^{-2}$, i.e. at the same ratio motivated by Noda & Done (2018). These results suggest that the structures of black hole accretion flows directly scale across a factor of $\sim 10^8$ in black hole mass and across different accretion states. Using Ruan et al. (2019) as a guide, there are potentially three accretion regimes: (i) a 'High/Soft State' with $\eta_{\rm Edd} \gtrsim -1$; (ii) a 'Low/Hard State' with $-2 \lesssim \eta_{\rm Edd} \lesssim -1$; and (iii) a 'Low/Hard State' with $\eta_{\rm Edd} \lesssim -2$. These are given as shaded regions in Fig. 10.

Apart from J1205+3422 on MJD 58538 (the observation obtained in poor conditions) we see all the C IV CLQ epochs are above $L/L_{\rm Edd}$ $\sim$5 per cent. The spectrum for J1205+3422 on MJD 58538 has low SNR, so while this object could well have entered a 'low-state', this is difficult to conclusively confirm. Nevertheless, and taking the J1205+3422 spectrum at face-value, we note that all the C IV CLQs are above $\sim$1 per cent in Eddington luminosity and thus above the suggested 'Low/Hard State' boundary.

While we note there is interest in plotting these accretion rates, and motivation from Noda & Done (2018) and Ruan et al. (2019), we caution against overinterpretation at this juncture. The point of this paper was to report on three very interesting CLQs. Our object definitions are based on empirical, observed properties. The potential for physical connections of accretion physics across the large-range of mass-scales is tantalizing, but is left to future investigations.

5 CONCLUSIONS

In this paper, we have reported on three redshift $z > 2$ quasars with dramatic changes in their C IV emission lines, the first sample of changing-look quasars at high redshift. This is also the first time the changing-look behaviour has been seen in a high-ionization emission line.

(i) SDSS J1205+3422, J1638+2827, and J2228+2201 show interesting behaviour in their observed optical light curves, and subsequent spectroscopy shows significant changes in the C IV broad emission line, with both line collapse and emergence being displayed on rest-frame time-scales of $\sim$240–1640 d.

(ii) Where observed, the profile of the Ly α/N V emission complex also changes, and there is tentative evidence for changes in the Mg II line.

(iii) Although line measurements from the three quasars show large changes in the C IV line flux-line width plane, the quasars

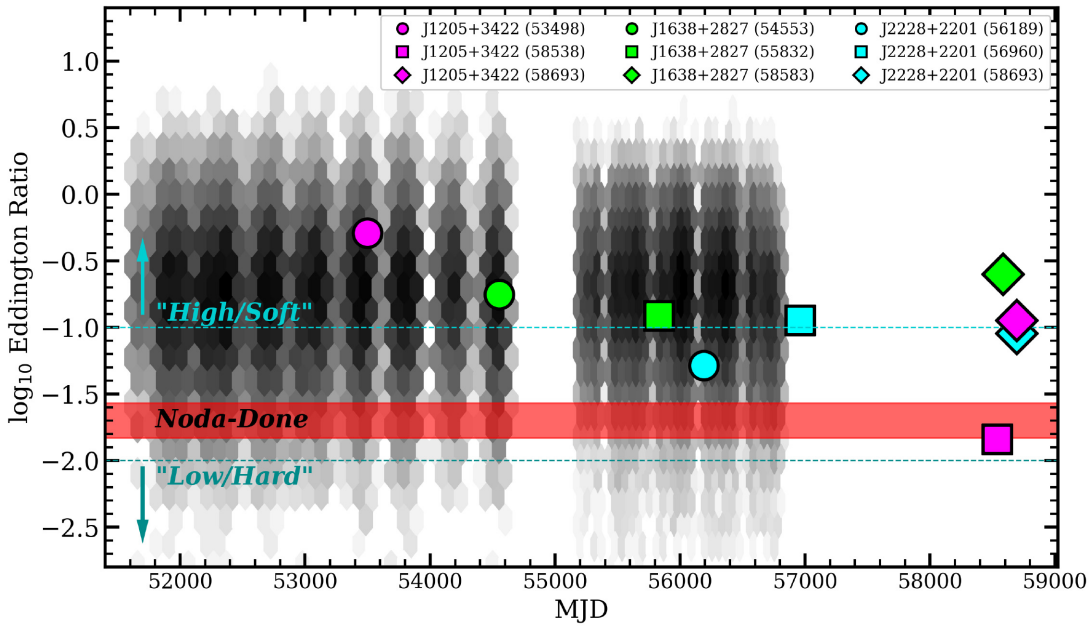

Figure 10. Eddington ratios of the three C IV CLQs. Gray scale gives the Eddington ratio ranges for quasars from SDSS Shen et al. (2011) and BOSS (Kozłowski 2017). Symbols as in Fig. 6. The red region ($L/L_{\rm Edd} \approx 0.02 \pm 0.01$; $\eta_{\rm Edd} = -1.7 \pm 0.13$) is the transition accretion rate suggested by Noda & Done (2018). A 'High/Soft State' with $\eta_{\rm Edd} \geq -1$ and a a 'Low/Hard State' with $\eta_{\rm Edd} \leq -2$ are indicated with dashed lines and arrows.

are not seen to be outliers when considered against the full quasar population in terms of (rest-frame) EW and FWHM properties.

(iv) We put these observations in context with recent 'state-change' models, and note that with the exception of the low SNR spectrum of J1205+3422 on MJD 58538, even in their low state, the C IV CLQs are above ∼5 per cent in Eddington luminosity.

There are now more observed examples of dramatic, dynamic changes in supermassive black hole systems, e.g. CLQs/CSQs, than there are Galactic X-ray Binaries. While the time-scales are expected to scale with black hole mass, whether the full physical system at large does, including the associated atomic physics, remains an open question.

Availability of data and computer analysis codes

All materials, data bases, data tables, and code are fully available at: `https://github.com/d80b2t/CIV_CLQs`.

ACKNOWLEDGEMENTS

We thank:

(i) Andy Lawrence, Mike Hawkins and David Homan for useful discussion;

(ii) the referee for a very constructive report that improved the paper;

NPR acknowledges support from the STFC and the Ernest Rutherford Fellowship scheme. MJG is supported in part by the NSF grants AST-1815034, and the NASA grant 16-ADAP16-0232.

This paper heavily used TOPCAT (v4.4) (Taylor 2005, 2011). This research made use of `Astropy`, a community-developed core Python package for Astronomy (Astropy Collaboration 2013; The Astropy Collaboration 2018). `pylustrator` (Gerum 2019) was also used.

Funding for SDSS-III has been provided by the Alfred P. Sloan Foundation, the Participating Institutions, the National Science Foundation, and the U.S. Department of Energy Office of Science. The SDSS-III web site is http://www.sdss3.org/. SDSS-III is managed by the Astrophysical Research Consortium for the Participating Institutions of the SDSS-III Collaboration including the University of Arizona, the Brazilian Participation Group, Brookhaven National Laboratory, Carnegie Mellon University, University of Florida, the French Participation Group, the German Participation Group, Harvard University, the Instituto de Astrofisica de Canarias, the Michigan State/Notre Dame/JINA Participation Group, Johns Hopkins University, Lawrence Berkeley National Laboratory, Max Planck Institute for Astrophysics, Max Planck Institute for Extraterrestrial Physics, New Mexico State University, New York University, Ohio State University, Pennsylvania State University, University of Portsmouth, Princeton University, the Spanish Participation Group, University of Tokyo, University of Utah, Vanderbilt University, University of Virginia, University of Washington, and Yale University.

This publication makes use of data products from the *Wide-field Infrared Survey Explorer*, which is a joint project of the University of California, Los Angeles, and the Jet Propulsion Laboratory/California Institute of Technology, and *NEOWISE*, which is a project of the Jet Propulsion Laboratory/California Institute of Technology. *WISE* and *NEOWISE* are funded by the National Aeronautics and Space Administration.

Based on observations obtained with the Samuel Oschin 48-inch Telescope at the Palomar Observatory as part of the Zwicky Transient Facility project. ZTF is supported by the National Science Foundation under Grant No. AST-1440341 and a collaboration including Caltech, IPAC, the Weizmann Institute for Science, the Oskar Klein Center at Stockholm University, the University of Maryland, the University of Washington, Deutsches Elektronen-Synchrotron and Humboldt University, Los Alamos National Laboratories, the TANGO Consortium of Taiwan, the University of Wisconsin at Mil-

waukee, and Lawrence Berkeley National Laboratories. Operations are conducted by COO, IPAC, and UW.

NPR dedicates this work, and indeed his previous research, to his father. Dad had a deep love for science, mathematics, and questioning the conventional wisdom. His support allowed me to become an astrophysicist and to have the adventures and discoveries we did. He is sorely missed.

REFERENCES

Abazajian K. N. et al., 2009, ApJS, 182, 543
Abolfathi et al., 2018, ApJS, 235, 42
Abramowicz M. A., Czerny B., Lasota J. P., Szuszkiewicz E., 1988, ApJ, 332, 646
Alam S. et al., 2015, ApJS, 219, 12
Alloin D., Pelat D., Phillips M., Whittle M., 1985, ApJ, 288, 205
Antonucci R., 2018, Nat. Astron., 2, 504
Astropy Collaboration et al., 2013, A&A, 558, A33
Baldwin J. A., 1977, ApJ, 214, 679
Barth A. J. et al., 2011, ApJ, 743, L4
Bellm E. C. et al., 2019a, PASP, 131, 018002
Bellm E. C. et al., 2019b, PASP, 131, 068003
Bian W.-H., Fang L.-L., Huang K.-L., Wang J.-M., 2012, MNRAS, 427, 2881
Calderone G. et al., 2017, MNRAS, 472, 4051
Chen Z.-F., Yi S.-X., Pang T.-T., Chen Z.-G., Gui R.-J., Wang Z.-W., Mo X.-H., Yi T.-F., 2019, ApJS, 244, 36
Coatman L., Hewett P. C., Banerji M., Richards G. T., Hennawi J. F., Prochaska J. X., 2017, MNRAS, 465, 2120
Cutri R. M. et al., 2011, Technical report, Explanatory Supplement to the WISE Preliminary Data Release Products. IPAC/Caltech
Cutri R. M. o., 2013, Technical report, Explanatory Supplement to the AllWISE Data Release Products. IPAC/Caltech
Dawson K. et al., 2013, AJ, 145, 10
Dawson K. S. et al., 2016, AJ, 151, 44
Denney K. D., 2012, ApJ, 759, 44
Dexter J., Agol E., 2011, ApJ, 727, L24
Doan A. N. et al., 2019, American Astronomical Society Meeting Abstracts #233. p. 242.23, https://ui.adsabs.harvard.edu/abs/2019AAS...23324223D
Dopita M. A., Sutherland R. S., 2003, Astrophysics of the Diffuse Universe, Springer
Drake A. J. et al., 2009, ApJ, 696, 870
Drake A. J. et al., 2013, ApJ, 763, 32
Dyer J. C., Dawson K. S., du Mas des Bourboux H., Vivek M., Bizyaev D., Oravetz A., Pan K., Schneider D. P., 2019, ApJ, 880, 78
Ebrero J. et al., 2016, A&A, 587, A129
Eisenstein D. J. et al., 2011, AJ, 142, 72
Elvis M., 2000, ApJ, 545, 63
Fausnaugh M. M. et al., 2016, ApJ, 821, 56
Fukugita M., Ichikawa T., Gunn J. E., Doi M., Shimasaku K., Schneider D. P., 1996, AJ, 111, 1748
Gaskell C. M., 1982, ApJ, 263, 79
Gerum R., 2019, preprint (arXiv:1910.00279v2)
Goad M. R., Korista K. T., Knigge C., 2004, MNRAS, 352, 277
Graham M. J. et al., 2015a, MNRAS, 453, 1562
Graham M. J. et al., 2015b, Nature, 518, 74
Graham M. J., Djorgovski S. G., Drake A. J., Mahabal A. A., Chang M., Stern D., Donalek C., Glikman E., 2014, MNRAS, 439, 703
Graham M. J., Djorgovski S. G., Drake A. J., Stern D., Mahabal A. A., Glikman E., Larson S., Christensen E., 2017, MNRAS, 470, 4112
Graham M. J. et al., 2019, PASP, 131, 078001
Graham M. J. et al., 2020, MNRAS, 491, 4925
Grier C. J. et al., 2019, ApJ, 887, 38
Guo H., Sun M., Liu X., Wang T., Kong M., Wang S., Sheng Z., He Z., 2019, ApJ, 883, L44
Hamann F., Ferland G., 1999, ARA&A, 37, 487
Hamann F. et al., 2017, MNRAS, 464, 3431
Hemler Z. S. et al., 2019, ApJ, 872, 21
Homan D., MacLeod C. L., Lawrence A., Ross N. P., Bruce A., 2020, MNRAS, 496, 309
Horne K. et al., 2020, preprint (arXiv:2003.01448)
Hutchinson T. A. et al., 2016, AJ, 152, 205
Jensen T. W. et al., 2016, ApJ, 833, 199
Kaiser N. et al., 2010, in Stepp L. M., Gilmozzi R., Hall H. J., eds, Proc. SPIE Conf. Ser. Vol. 7733, Society of Photo-Optical Instrumentation Engineers (SPIE), SPIE, Bellingham, p. 77330E
Kozłowski S., 2017, ApJS, 228, 9
Kramida A., Ralchenko Y., Reader J., NIST ASD Team, 2018, National Institute of Standards and Technology, Gaithersburg, MD
Kramida A., Ralchenko Yu., Reader J., and NIST ASD Team, 2019, NIST Atomic Spectra Database (ver. 5.7.1). National Institute of Standards and Technology, Gaithersburg, MD, [Online]. Available: https://physics.nist.gov/asd [2019, November 7]
LaMassa S. M. et al., 2015, ApJ, 800, 144
Lawrence A., 2018, Nat. Astron., 2, 102
Leighly K. M., 2004, ApJ, 611, 125
Lightman A. P., Eardley D. M., 1974, ApJ, 187, L1
MacLeod C. L. et al., 2012, ApJ, 753, 106
MacLeod C. L. et al., 2019, ApJ, 874, 8
Magnier E. A. et al., 2013, ApJS, 205, 20
Mahabal A. A. et al., 2011, Bull. Astron. Soc. India, 39, 387
Mainzer A. et al., 2011, ApJ, 731, 53
Margala D., Kirkby D., Dawson K., Bailey S., Blanton M., Schneider D. P., 2016, ApJ, 831, 157
Masci F. J. et al., 2019, PASP, 131, 018003
Matthews T. A., Sandage A. R., 1963, ApJ, 138, 30
McKernan B., Ford K. E. S., Kocsis B., Lyra W., Winter L. M., 2014, MNRAS, 441, 900
McKernan B. et al., 2018, ApJ, 866, 66
Mejía-Restrepo J. E., Trakhtenbrot B., Lira P., Netzer H., Capellupo D. M., 2016, MNRAS, 460, 187
Mejía-Restrepo J. E., Trakhtenbrot B., Lira P., Netzer H., 2018, MNRAS, 478, 1929
Meyer R. A., Bosman S. E. I., Ellis R. S., 2019, MNRAS, 487, 3305
Murray N., Chiang J., Grossman S. A., Voit G. M., 1995, ApJ, 451, 498
Myers A. D. et al., 2015, ApJS, 221, 27
Noda H., Done C., 2018, MNRAS, 480, 3898
Oke J. B., Gunn J. E., 1983, ApJ, 266, 713
Oke J. B. et al., 1995, PASP, 107, 375
Pâris I. et al., 2018, A&A, 613, A51
Pâris I., Petitjean P., Ross N. P. et al., 2017, A&A, 597, A79
Peterson B. M., 1997, An Introduction to Active Galactic Nuclei. Cambridge University Press, Cambridge
Pogge R. W., Peterson B. M., 1992, AJ, 103, 1084
Proga D., Stone J. M., Kallman T. R., 2000, ApJ, 543, 686
Rakić N., La Mura G., Ilić D., Shapovalova A. I., Kollatschny W., Rafanelli P., Popović L. Č., 2017, A&A, 603, A49
Rasmussen C. E., Williams C. K. I., 2006, Gaussian Processes for Machine Learning. The MIT Press, Cambridge, MA
Richards G. T. et al., 2002, AJ, 123, 2945
Richards G. T. et al., 2006, ApJS, 166, 470
Richards G. T. et al., 2011, AJ, 141, 167
Ross N. P. et al., 2012, ApJS, 199, 3
Ross N. P. et al., 2015, MNRAS, 453, 3932
Ross N. P. et al., 2018, MNRAS, 480, 4468
Ruan J. J., Anderson S. F., Eracleous M., Green P. J., Haggard D., MacLeod C. L., Runnoe J. C., Sobolewska M. A., 2019, preprint (arXiv:1903.02553v1)
Runnoe J. C., Brotherton M. S., Shang Z., DiPompeo M. A., 2013, MNRAS, 434, 848
Schlafly E. F., Finkbeiner D. P., 2011, ApJ, 737, 103
Schneider D. P. et al., 2010, AJ, 139, 2360
Shakura N. I., Sunyaev R. A., 1973, A&A, 24, 337
Shen Y. et al., 2011, ApJS, 194, 45
Shen Y. et al., 2015, ApJS, 216, 4
Shen Y. et al., 2019, ApJS, 241, 34

Shen Y., Greene J. E., Strauss M. A., Richards G. T., Schneider D. P., 2008, ApJ, 680, 169
Shields J. C., 2007, in Ho L. C., Wang J. W., eds, ASP Conf. Ser. Vol. 373, The Central Engine of Active Galactic Nuclei. Astron. Soc. Pac., San Francisco, p. 355
Smee S. A. et al., 2013, AJ, 146, 32
Stern D. et al., 2017, ApJ, 839, 106
Stern D. et al., 2018, ApJ, 864, 27
Stoughton C. et al., 2002, AJ, 123, 485
Stubbs C. W. et al., 2010, ApJS, 191, 376
Sun M., Xue Y., Richards G. T., Trump J. R., Shen Y., Brandt W. N., Schneider D. P., 2018, ApJ, 854, 128
Taylor M. B., 2005, in Shopbell P., Britton M., Ebert R., eds, ASP Conf. Ser. Vol. 347, Astronomical Data Analysis Software and Systems XIV. Astron. Soc. Pac., San Francisco, p. 29
Taylor M., 2011, TOPCAT: Tool for OPerations on Catalogues And Tables, Astrophysics Source Code Library, record ascl:1101.010
The Astropy Collaboration, 2018, preprint (arXiv:1801.02634v2)
Tonry J. L. et al., 2012, ApJ, 750, 99
Trakhtenbrot B. et al., 2019, ApJ, 883, 94
Vestergaard M., Peterson B. M., 2006, ApJ, 641, 689
Wilhite B. C., Vanden Berk D. E., Brunner R. J., Brinkmann J. V., 2006, ApJ, 641, 78
Wright E. L. et al., 2010, AJ, 140, 1868
Yao S. et al., 2019, ApJS, 240, 6
York D. G. et al., 2000, AJ, 120, 1579
Zakamska N. L. et al., 2016, MNRAS, 459, 3144
Zakamska N. L. et al., 2019, MNRAS, 489, 497

This paper has been typeset from a TEX/LATEX file prepared by the author.